

High-Performance Polymer Solar Cells with Zinc Sulfide-Phenanthroline Derivatives as the Hybrid Cathode Interlayers

Yulei Wu,[†] Xiaohui Liu,^{†,‡} Xiaodong Li,^{†,‡} Wenjun Zhang,[†] Hai-Qiao Wang,^{*,†} and Junfeng Fang^{*,†}

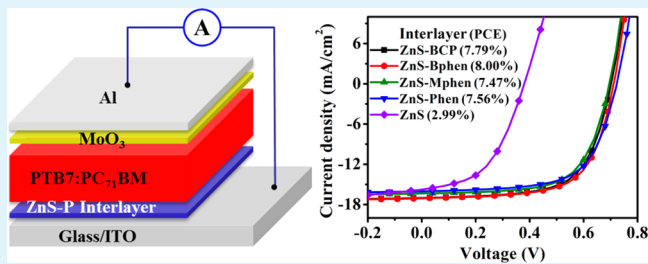
[†]Ningbo Institute of Materials Technology and Engineering, Chinese Academy of Sciences, Ningbo 315201, China

[‡]University of Chinese Academy of Sciences, Beijing 100049, China

Supporting Information

ABSTRACT: Environmentally benign hybrid interlayers are prepared by modifying the zinc sulfide (ZnS) with phenanthroline/derivatives and utilized in inverted polymer solar cells (PSCs). Performances of the inverted PSCs are improved enormously by incorporating these hybrid interlayers, as which can effectively improve the energy level alignment, electron mobility, surface morphology, and interfacial contact. Greatly improved power conversion efficiencies (PCEs) of 7.79%, 8.00%, 7.47%, and 7.56% are achieved with these hybrid interlayers ZnS-BCP, ZnS-Bphen, ZnS-Mphen, and ZnS-Phen, respectively, compared to the PCE of 2.99% of the reference ZnS-based device, based on PTB7:PC₇₁BM active layer. Our results demonstrate that hybrid interfacial materials comprising inorganic and organic semiconductor possess promising potential to improve the performance of organic electronic devices, and set an example to develop this novel class of interfacial materials for electronic devices.

KEYWORDS: *inverted polymer solar cells, cathode, hybrid interlayer, ZnS, phenanthroline*



1. INTRODUCTION

Polymer solar cells (PSCs) based on donor–acceptor blend bulk heterojunctions (BHJ) have been studied widely because of their promising advantages, such as low-cost, flexible form, light weight, and ease of large area fabrication.^{1–3} The power conversion efficiency (PCE) of PSCs has been dramatically improved and is approaching ~10% in the scientific literatures.^{4–7} These improvements derived not only from the continuous emergence of novel donor materials but also from the great progresses achieved in the interface studies.^{8–10} The commercial hole-transport material, poly(3,4-ethylenedioxythiophene):poly(styrenesulfonate) (PEDOT:PSS) is commonly used as anode interface material in conventional device architecture, aiming to improve the surface property of indium–tin oxide (ITO) electrode and its work function (WF). While the strong acidic nature of which can result in ITO erosion and seriously affect the device stability.^{10,11} Hence, many new anode interface materials, such as MoO₃, V₂O₅, WO₃, and NiO, etc., have been explored for substitution.^{12–15} Meanwhile, cathode interface materials, such as TiO₂, ZnO, PFN, FTBTFT-N, etc., become more attractive recently since they can render the device in more stable inverted architecture.^{4,7,16,17}

Generally, these interface materials can be classified into three categories: organic, inorganic, and hybrid interlayers. Most studies have focused on the first two, while quite limited studies have been reported about the hybrid type. Recently, the hybrid interfacial materials draw great attention from researchers since they presented promising potential as

interface layer in photovoltaics,^{18–24} because of their combinatorial favorable properties of organic and inorganic semiconductors. Although impressive performances have been obtained for devices fabricated with ZnO-C60, ZnO/CsSt, and CdS-BCP hybrid cathode interlayers,^{6,25,26} great efforts still need to be conducted to explore this hybrid type interlayers.

Zinc sulfide (ZnS) is an environmentally friendly semiconductor with a wide direct bandgap (>3.5 eV), which is a promising material that has vast potential in thin film devices, such as photoluminescent and electroluminescent devices.^{27–29} Meanwhile, high electron mobility as well as high electron affinity makes it attractive as an electron acceptor in hybrid bulk heterojunction photovoltaic devices, such as polymer:ZnS hybrid bulk heterojunction solar cells.^{30,31} However, there are few literatures focusing on ZnS or its hybrid interfacial materials have been reported in PSCs.^{32,33}

In this study, we fabricated BHJ polymer solar cells based on poly[[4,8-bis[(2-ethylhexyl)oxy]benzo[1,2-b:4,5-b']-dithiophene-2,6-diyl][3-fluoro-2-[(2-ethylhexyl)carbonyl]thieno[3,4-b]thiophenediyl]] (PTB7) and [6,6]-phenyl-C₇₁-butyric acid methyl ester (PC₇₁BM) as the active layer, and hybrid ZnS-phenanthroline/derivatives (ZnS-P) as the cathode buffer layer grown *in situ* from its chelate precursor zinc ethylxanthate ($Zn(S_2COEt)_2$).³⁴ By which, optimal PCE up to 8.00% is achieved for devices with configuration ITO/ZnS-P/

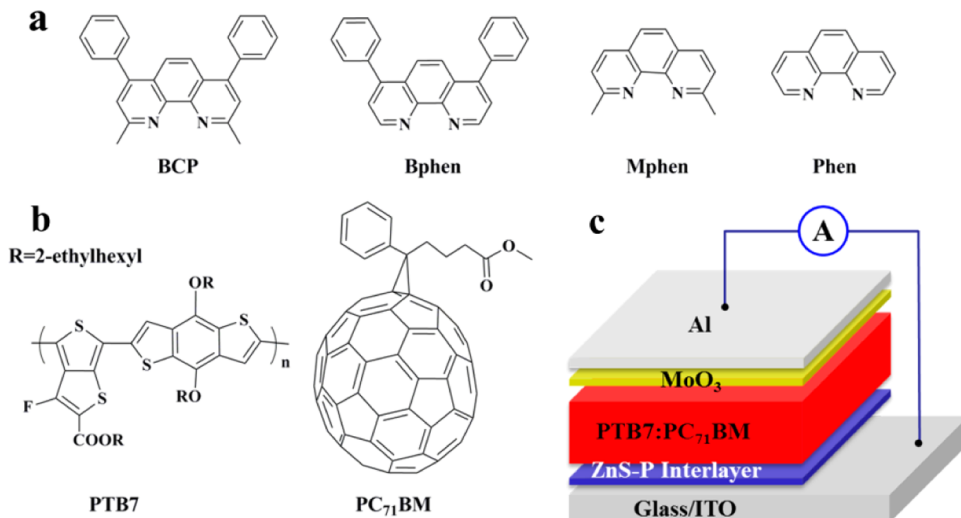


Figure 1. (a) Molecular structures of phenanthroline derivatives BCP, Bphen, Mphen, and Phen. (b) Molecular structures of PTB7 and PC₇₁BM. (c) Inverted device structure of ITO/ZnS-P/PTB7:PC₇₁BM/MoO₃/Al.

PTB7:PC₇₁BM/MoO₃/Al, because of the improved interface properties by hybrid ZnS-P. While with the pure ZnS cathode interlayer, only 2.99% of PCE is obtained this technique.

2. EXPERIMENTAL SECTION

2.1. Materials and Methods. Zn(Ac)₂, KS₂COEt, and pyridine were bought from Aladdin Reagent. Phenanthroline derivatives including 2,9-dimethyl-4,7-diphenyl-1,10-phenanthroline (BCP), 4,7-diphenyl-1,10-phenanthroline (Bphen), 2,9-dimethyl-1,10-phenanthroline (Mphen), and 1,10-phenanthroline (Phen) were bought from Alfa Aesar. PTB7 and PC₇₁BM were purchased from 1-Material Chemscitech Inc. (Canada) and American Dye Source Inc. (ADS), respectively. All the available materials were used as received without any further purification.

The preparation of zinc xanthate (Zn(S₂COEt)₂) was described in the literatures.^{34,35} BCP, Bphen, Mphen, and Phen were added into a stirred suspension of Zn(S₂COEt)₂ in chloroform, respectively, and the suspension immediately vanished when phenanthroline derivative was added in. The yellow solution was stirred for 2 h and then filtrated. The obtained filtrates were left to crystallize by slow evaporation. And then the crude product of Zn(S₂COEt)₂(P) was purified by recrystallization from chloroform twice.

2.2. Device Fabrication. The solar cells were fabricated on glass substrates with ITO ($10 \Omega \text{ sq}^{-1}$) patterned on the surface. The ITO substrates were cleaned by sequential ultrasonic treatment in detergent, deionized water, acetone, and isopropanol for 20 min each. Finally the substrates were dried with pressurized flowing nitrogen gas and then irradiated in a UV-ozone chamber for 20 min. The precursors Zn(S₂COEt)₂(P) (dissolved in N,N-dimethylformamide, DMF, 20 mg/mL) were spin-coated onto the ITO substrates under 5000 rpm for 60 s and then annealed at 175 °C for 30 min in air. Then the substrates were transferred into an argon-filled glovebox and the active layer (~96 nm) was deposited onto the interfacial layer by spin-coating PTB7:PC₇₁BM dissolved in mixed solvents of chlorobenzene/1,8-diiodooctane (97:3 vol %) at 2000 rpm for 120 s. The blend ratio of PTB7:PC₇₁BM was 1:1.5 by weight (25 mg/mL). The device fabrication was completed by thermal evaporation of 10 nm of MoO₃ and 100 nm of Al as the anode under vacuum at a pressure less than 2×10^{-6} Torr. The effective device area was 0.06 cm². The electron-only devices were made with the structure of ITO/ZnS(/ZnS-P)/PTB7:PC₇₁BM/LiF(1 nm)/Al.

2.3. Device Characterization. J-V characteristics of PSCs were performed in glovebox using a Keithley 2440 sourcemeter under a simulated AM1.5G spectrum with an Oriel Sol3A solar simulator. The external quantum efficiency (EQE) measurements were performed using a Newport quantum efficiency measurement system (ORIEL

IQE 200TM) with a lock-in amplifier and 150 W xenon lamp without encapsulation in air. The light intensity at each wavelength was calibrated with a standard single-crystal Si/Ge photovoltaic cell.

X-ray photoelectron spectroscopy (XPS) and Ultraviolet photo-electron spectroscopy (UPS) measurements were carried out using a Kratos AXIS ULTRA DALD XPS/UPS system. For XPS, survey scans to identify overall surface composition were recorded using a monochromatic Al K α X-ray source (1486.6 eV). High-resolution scans to identify bonding states were performed at 20 eV pass energy and 50 meV channel width. All the spectra were adjusted according to the standard value of C 1s peak at 284.8 eV. UPS was performed using He I radiation at 21.21 eV from a discharge lamp operated at 20 mA, a pass energy of 5 eV, and a channel width of 25 meV. A -7.35 V bias was applied to the samples to separate the sample and analyzer low-kinetic-energy cutoffs.

UV-vis spectra of quartz/active layer or quartz/ZnS (or ZnS-Bphen)/active layer were tested on a UV-3300 spectrophotometer (MAPADA Co. Ltd. Shanghai China). Droplet images were recorded on a contact-angle system (model OCA20) and the film thickness was measured under Veeco Dektak 150. The surface morphology of the interlayers were investigated using a field-emission scanning electron microscope (FE-SEM) (Hitachi S-4800) and an atomic force microscope (AFM) with tapping mode using a Veeco dimension V atomic microscope at room temperature.

3. RESULTS AND DISCUSSION

In this study, the phenanthroline derivatives including BCP, Bphen, Mphen, and Phen were utilized as organic ligands to coordinate ZnS(S₂COEt) to prepared zinc chelate compound precursors. With the annealing process, hybrid cathode interlayers, such as ZnS-BCP, ZnS-Bphen, ZnS-Mphen, and ZnS-Phen were formed by decomposing the precursors of ZnS(S₂COEt)(P) on the ITO substrates. The as-prepared hybrid cathode films were about 25 nm measured with a profiler. Figure 1a depicts the molecular structures of BCP, Bphen, Mphen and Phen. The chemical structures of photoactive materials (PTB7 and PC₇₁BM) and the configuration of the inverted PSCs are also presented in Figure 1b and 1c, respectively. The 10 nm MoO₃ deposited on top of the photoactive layer is used to facilitate the hole collection.

Device characterizations of the PSCs incorporating ZnS and hybrid ZnS-P as cathode interlayers are presented in terms of current density versus voltage (J-V) under 100 mW/cm² air mass 1.5 global (AM 1.5G) in Figure 2. With hybrid interlayers,

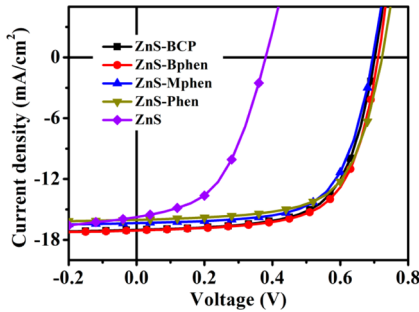


Figure 2. Current–voltage (J – V) characteristics of the PSCs based on different cathode interlayers (ZnS-P and ZnS) under AM 1.5G irradiation (100 mW/cm^2). The device structure is ITO/ZnS-P/ZnS/PTB7:PC₇₁BM/MoO₃/Al.

greatly enhanced performances are obtained for all the devices compared to the reference device with ZnS interlayer because of the huge enhancement in open-circuit voltage (V_{oc}) and fill factor (FF), and slight increase in short-circuit current density (J_{sc}). The device using ZnS as the cathode interfacial layer shows V_{oc} of 0.371 V, J_{sc} of 16.07 mA/cm^2 , and FF of 50.09%, corresponding to PCE of 2.99%. While the ZnS-P interlayers promote the V_{oc} to $\sim 0.7 \text{ V}$, J_{sc} to $\sim 16\text{--}17 \text{ mA/cm}^2$, and FF to $>65\%$, resulting in PCEs over 7.50%. And the best PCE 8.00% is achieved with ZnS-Bphen hybrid interfacial layer as which provides the highest J_{sc} and FF simultaneously keeping a high V_{oc} . The corresponding device parameters including average values are summarized in Table 1. Furthermore, the statistical data are presented in the form of a standard box plot to analyzing the statistical distributions of device parameters (see Figure S1). Compared with other hybrid ZnS-P devices, large differences in parameters (FF and J_{sc}) of ZnS-Mphen devices were recorded, which should be originated from the singular data point of device due to improper fabrication or test (such as poor probe contact). To understand the enhancement, the series resistance (R_s) and shunt resistance (R_{sh}) of the PSCs with different cathode interlayers are also summarized in Table 1. Much lowered R_s are observed for devices with hybrid interlayers, indicating better ohmic contact formation between the active layer and the cathode compared to the reference device. And meanwhile, almost 4 times higher R_{sh} are determined for hybrid interlayer based devices, suggesting lower trap density and depressed recombination rate at the interface.^{36–38} Both can promote the charge collection efficiency, and which is consistent with the measured device parameters.

To further understand the underlying mechanisms for the improvement of the devices, dark J – V curves were measured. In dark condition, as shown in Figure 3, the devices with hybrid interlayers exhibit a turn-on voltage of about 0.8–0.9 V while it

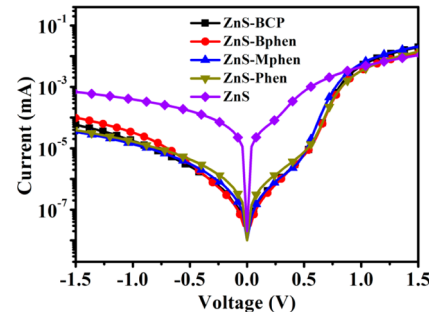


Figure 3. J – V characteristics of the PSCs devices based on different cathode interlayers (ZnS-P and ZnS) under dark conditions.

was only 0.5–0.6 V for the control device, implying that the built-in potential across the device, which is the upper limit of the attainable V_{oc} in PSCs,³⁹ considerably increased upon utilization of the hybrid cathode interlayers. In addition, the leakage current of the devices with a hybrid interlayer is significantly restrained. Simultaneously, the diode rectification ratio characterized at $\pm 1.5 \text{ V}$ was 1–2 orders higher than that of the control device, which indicates that the recombination was greatly suppressed. Furthermore, hole-blocking and electron-collecting become more efficient when the hybrid ZnS-P cathode buffer layers are used. Thus, higher performance devices can be expected when hybrid cathode buffer layers are utilized.

Figure 4 shows the energy level diagrams of constituents used in the fabricated inverted PSCs. To achieve higher

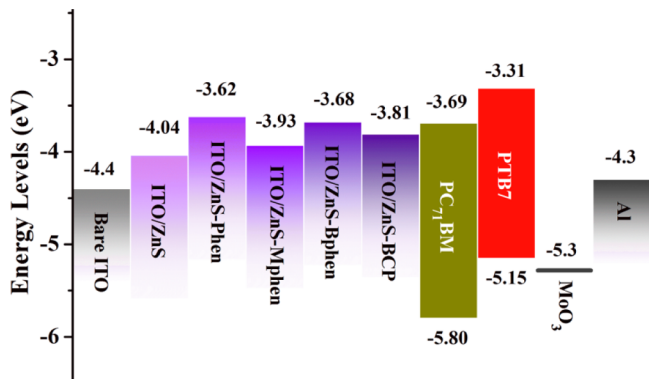


Figure 4. Energy level diagrams of materials used in the inverted device configuration. Work function of ZnS, ZnS-P, and bare ITO were measured by UPS, and the rest were obtained from relevant literatures.

efficiency of our PSCs, well-matched energy levels between the work functions of ZnS-with/without organic ligands and the lowest unoccupied molecular orbital (LUMO) of PC₇₁BM are

Table 1. Photovoltaic Performance of PSCs Based on Different Cathode Interlayers (ZnS-P and ZnS) under AM 1.5G Irradiation (100 mW/cm²)

interlayer	V_{oc} (V)	J_{sc} (mA/cm^2)	FF (%)	PCE (%)	R_s ($\Omega \cdot \text{cm}^2$)	R_{sh} ($\text{k}\Omega \cdot \text{cm}^2$)
ZnS-BCP	0.702	17.03	65.16	7.79 (7.55 ± 0.16) ^a	4.94	0.77
ZnS-Bphen	0.711	17.08	65.88	8.00 (7.62 ± 0.20) ^a	5.12	0.94
ZnS-Mphen	0.695	16.33	65.81	7.47 (7.24 ± 0.22) ^a	5.09	1.23
ZnS-Phen	0.723	16.05	65.15	7.56 (7.37 ± 0.16) ^a	5.01	0.76
ZnS	0.371	16.07	50.09	2.99 (2.94 ± 0.03) ^a	7.08	0.25

^aThe average PCEs were based on 14 individual devices.

required. The work functions of bare ITO and hybrid ZnS-P interlayers were measured by UPS (Figure S2). The energy levels of the rest materials in Figure 4 were obtained from relevant literatures.^{40–42} In our study, there was almost no photovoltaic behavior detected for devices using the bare ITO as the cathode directly. As shown in the diagram, reduced work function of the cathode is achieved by inserting each of the hybrid interlayers due to the high LUMO of organic molecules, which decreases the energy gap between the Fermi-level of the electrode and the LUMO of the PC₇₁BM, thus benefit the electron transport from PC₇₁BM to the cathode, as evidenced by results of the *J*–*V* measurements. Considering the small difference between the LUMO levels of ZnS-P and ZnS interlayer, and the hugely improved *V*_{oc} of the ZnS-P devices compared to the ZnS device, we consider the enhancement in *V*_{oc} is not mainly caused by the reduced work function of the cathode but mainly by the depressed charge recombination in devices contributed from the largely improved shunt resistance, film morphology, and contact properties between layers, introduced by the ZnS-P interlayers.

To better understand the enhancement of device performance upon the incorporation of the hybrid ZnS-P interlayers, the apparent charge carrier transport properties were evaluated by using electron-only devices (Figure S3) according to the space charge limited current (SCLC) model (Figure S4).^{39,43,44} The electron-only device structure was ITO/ZnS (/ZnS-P)/PTB7:PC₇₁BM/LiF/Al. The apparent electron mobilities were determined to be 1.29×10^{-3} , 1.54×10^{-3} , 1.57×10^{-5} , and $3.69 \times 10^{-6} \text{ cm}^2 \cdot \text{V}^{-1} \cdot \text{s}^{-1}$ for ZnS-BCP, ZnS-Bphen, ZnS-Mphen, and ZnS-Phen based devices, and $1.18 \times 10^{-6} \text{ cm}^2 \cdot \text{V}^{-1} \cdot \text{s}^{-1}$ for the reference ZnS-based devices. Obviously, devices with ZnS-BCP and ZnS-Bphen showed higher apparent electron mobility than that of the reference device. Three orders of magnitude of the apparent electron mobility were recorded since they possess more rigid and planar phenyl groups (Figure 1), which could have improved the intermolecular packing and provided more extended π -electrons, thus contributing to the electron mobility.^{45,46} These improved charge transport properties are also consistent with their improved *J*_{sc} (Table 1). While the other hybrid materials showed comparative apparent mobility properties compared to the reference ZnS because of the different molecular structure. And this is reflected by their recorded similar *J*_{sc} values compared to that of the reference device. Although similar *J*_{sc} were recorded in the ZnS-Phen and ZnS devices, much higher PCE was obtained for the device with ZnS-Phen compared with the ZnS device. We consider this to be the result of improvements in other parameters of the devices like smaller *R*_s, larger *R*_{sh}, better matched energy levels, improved contacting property between layers and so on by the hybrid interlayers.

UV-vis spectra were measured to identify the absorption of components in devices with or without interlayer (ZnS or ZnS-Bphen). Since the enhancement of absorption devoted by the interlayers was not obvious, as presented in Figure S5. Thus, the improvement of the photocurrent density should be mainly ascribed to the improved carrier transport and collection. The EQE curves of the devices with different interlayer are presented in Figure S6. The integrating photocurrent densities are consistent with the corresponding *J*_{sc}. EQEs of hybrid interlayer based devices show higher value than the ZnS-based device in the wavelength range 400–700 nm. According to the steady absorption spectra (Figure S5), we consider this

enhancement is due to the improved interface properties at the cathode by the hybrid interlayers.

Moreover, the influence on the surface characteristics of the cathode interlayers by the different hybrid materials were also investigated through SEM and AFM measurements. Figure 5

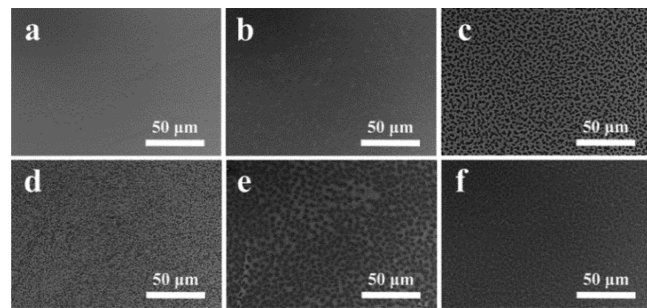


Figure 5. SEM images of bare ITO and different cathode interlayer (ZnS and ZnS-P): (a) bare ITO, (b) ZnS, (c) ZnS-BCP, (d) ZnS-Bphen, (e) ZnS-Mphen, and (f) ZnS-Phen.

displays the SEM images of the ZnS and ZnS-P interlayer surface. The ZnS film (Figure 5b) shows very similar surface characteristic like the bare ITO (Figure 5a) due to its good spreadability on ITO substrate. However, distinct surface morphologies are observed when ZnS is modified by phenanthroline and its derivatives (Figure 5c–f), where well distributed aggregations are observed. Similar results are also observed in the topography AFM images (Figure S7), in which domains with height of 20–30 nm are recorded (Figure S7b–f). We consider these different aggregations could have been resulted from the different molecular polarity and planarity of the organic molecules. As shown in Figure 1a, two separated methyl groups are contained in the Mphen molecule, two rigid phenyl groups are included in the Bphen molecule, and both methyl and phenyl side groups exist in the BCP molecule. These different side groups can provide different polarity and planarity for the corresponding molecules which results in different steric hindrance, hence different aggregations. And we speculate that the more methyl and phenyl groups could have contributed to the larger aggregations for the ZnS-BCP, ZnS-Bphen, and ZnS-Mphen films. Moreover, when the ZnS was modified by phenanthroline and its derivatives, the PTB7:PC₇₁BM films on these hybrid interlayers exhibited slightly smoother surface with root-mean-square (RMS) roughness of 1.09, 1.12, 1.19, and 1.20 nm, respectively (Figure S8). Especially for ZnS-BCP and ZnS-Bphen, relatively smaller domain and smoother film surface were observed, which is consistent with the obtained device performances.

Furthermore, the enhanced hydrophobicity of the hybrid interlayer surface was confirmed by the increased water contact angles compared to the corresponding value of the ZnS film (Figure 6). The water contact angle was increased from 47° of the pristine ZnS film to 74°, 70°, 61°, and 66° of the ZnS-BCP, ZnS-Bphen, ZnS-Mphen, and ZnS-Phen hybrid films, respectively. In the hybrid films, nitrogen atoms with higher electronegativity chelating the ZnS toughly while the aromatic ring with lower electronegativity existed oriented upward made the films hydrophobic and compatible with nonpolar chlorobenzene solvent. Especially, in the film of ZnS-BCP and ZnS-Bphen (Figure 6c, d), the existence of diphenyl groups made them more hydrophobic than the rest ZnS-Mphen and ZnS-Phen (Figure 6e, f). Obviously, modification by organic

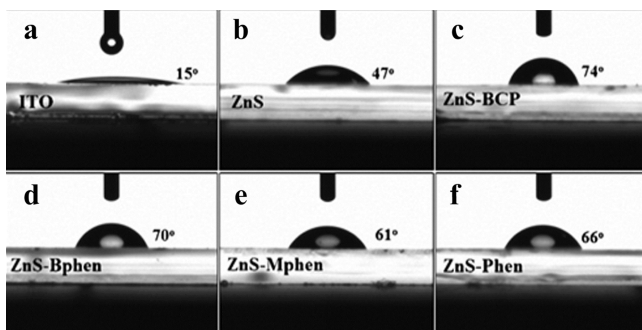


Figure 6. Contact angle measurements of water drop on (a) bare ITO (15°), (b) ZnS (47°), (c) ZnS-BCP (74°), (d) ZnS-Bphen (70°), (e) ZnS-Mphen (61°), and (f) ZnS-Phen (66°).

ligands increased the intimate contact between the interlayer and the active layer, leading to the improvement of the device performance.

The well-distributed domains as mentioned in Figure 5c–f should be the aggregates of the chelate compounds (ZnS-BCP, ZnS-Bphen, ZnS-Mphen, and ZnS-Phen). For detailed chemical state of the elements on film surface after modification, as an example, the ZnS-Bphen film surface was characterized by XPS. As shown in Figure S9a, the difference of the XPS survey spectra between ZnS decomposed from $Zn(S_2COEt)_2$ (pyridine) and ZnS-Bphen mainly lies in the peak of N. Figure S9b exhibits the Zn 2p peaks for chelate compound ZnS-Bphen where Zn binding energy was matched through peak deconvolution with the independent Zn–S (Zn 2p_{3/2} 1021.6 eV) and Zn–N (Zn 2p_{3/2} 1022.6 eV) chemical bonds.⁴³ The N–Zn peak (N 1s 398.5 eV) and N–C peak (N 1s 399.4 eV) in hybrid compound ZnS-Bphen were shown in Figure S9c. The shifts of Zn peak to higher BE and N peak to lower BE confirms the existence of coordination bonds between ZnS and Bphen, which is in agreement with the SEM images and contact angle results.

As demonstrated above, besides the different film morphologies, electron mobilities, diverse work function and surface affinity were recorded and different morphologies of the active layers were observed as well. We believe that all these aspects and together with other factors like the conducting properties of the ZnS-P layer, must have contributed to the device performance. And their balanced effects have determined the final outcome.

4. CONCLUSION

In conclusion, various ZnS-P hybrid interlayers were prepared using an in situ growth method for the inverted PSCs. We studied the performance of the inverted PSCs incorporating ZnS and hybrid ZnS-P interlayers (ZnS-BCP, ZnS-Bphen, ZnS-Mphen, ZnS-Phen) as cathode interlayers. The hybrid ZnS-P interlayers can effectively decrease the energy barrier, boost the electron mobility, and improve the morphology and interfacial contact properties. For the optimized inverted devices based on PTB7:PC₇₁BM incorporating the hybrid ZnS-P films, the PCE was significantly improved to 7.79%, 8.00%, 7.47%, and 7.56%, respectively, compared to the PCE 2.99% of the pristine ZnS-based device. These results demonstrate that the environmentally benign inorganic semiconductors like ZnS can be modified by organic semiconductors to produce a general applicable hybrid interfacial material for PSCs. Our work

suggests a promising potential for these hybrid semiconductors as interfacial materials in optoelectronic devices.

■ ASSOCIATED CONTENT

● Supporting Information

The Supporting Information is available free of charge on the ACS Publications website at DOI: [10.1021/acsami.5b10798](https://doi.org/10.1021/acsami.5b10798).

Details of the statistical data of device performance, UPS spectra, characteristic curves of electron-only devices and corresponding SCLC fitting results, UV-vis absorption spectra, EQE spectra, AFM images of interlayers surface and the photoactive layer, and XPS spectra ([PDF](#))

■ AUTHOR INFORMATION

Corresponding Authors

*E-mail: hqwang@nimte.ac.cn.

*E-mail: fangjf@nimte.ac.cn.

Author Contributions

Yulei Wu and Xiaohui Liu contributed equally to this work.

Notes

The authors declare no competing financial interest.

■ ACKNOWLEDGMENTS

This research was supported by National Natural Science Foundation of China (No. 61474125, 51502313), Zhejiang Provincial Natural Science Foundation of China (LR14E030002, LY16E02006), and Ningbo Science and Technology Bureau (2014B82010). The work was also supported by National Young Top-Notch Talent Program of China and Hundred Talent Program of Chinese Academy of Sciences.

■ REFERENCES

- (1) Chen, J.; Cao, Y. Development of Novel Conjugated Donor Polymers for High-Efficiency Bulk-Heterojunction Photovoltaic Devices. *Acc. Chem. Res.* **2009**, *42*, 1709–1718.
- (2) Günes, S.; Neugebauer, H.; Sariciftci, N. S. Conjugated Polymer-Based Organic Solar Cells. *Chem. Rev.* **2007**, *107*, 1324–1338.
- (3) Yu, G.; Gao, J.; Hummelen, J.; Wudl, F.; Heeger, A. Polymer Photovoltaic Cells: Enhanced Efficiencies via a Network of Internal Donor-Acceptor Heterojunctions. *Science* **1995**, *270*, 1789–1790.
- (4) Zhang, W.; Wu, Y.; Bao, Q.; Gao, F.; Fang, J. Morphological Control for Highly Efficient Inverted Polymer Solar Cells Via the Backbone Design of Cathode Interlayer Materials. *Adv. Energy Mater.* **2014**, *4*, 1400359.
- (5) You, J.; Dou, L.; Yoshimura, K.; Kato, T.; Ohya, K.; Moriarty, T.; Emery, K.; Chen, C.-C.; Gao, J.; Li, G.; et al. A Polymer Tandem Solar Cell with 10.6% Power Conversion Efficiency. *Nat. Commun.* **2013**, *4*, 1446.
- (6) Liao, S. H.; Jhuo, H. J.; Cheng, Y. S.; Chen, S. A. Fullerene Derivative-Doped Zinc Oxide Nanofilm as the Cathode of Inverted Polymer Solar Cells with Low-Bandgap Polymer (PTB7-Th) for High Performance. *Adv. Mater.* **2013**, *25*, 4766–4771.
- (7) He, Z.; Zhong, C.; Su, S.; Xu, M.; Wu, H.; Cao, Y. Enhanced Power-Conversion Efficiency in Polymer Solar Cells Using an Inverted Device Structure. *Nat. Photonics* **2012**, *6*, 591–595.
- (8) Li, G.; Zhu, R.; Yang, Y. Polymer Solar Cells. *Nat. Photonics* **2012**, *6*, 153–161.
- (9) Chen, L.-M.; Xu, Z.; Hong, Z.; Yang, Y. Interface Investigation and Engineering—Achieving High Performance Polymer Photovoltaic Devices. *J. Mater. Chem.* **2010**, *20*, 2575–2598.
- (10) Hau, S. K.; Yip, H.-L.; Acton, O.; Baek, N. S.; Ma, H.; Jen, A. K.-Y. Interfacial Modification to Improve Inverted Polymer Solar Cells. *J. Mater. Chem.* **2008**, *18*, 5113–5119.

- (11) Jørgensen, M.; Norrman, K.; Krebs, F. C. Stability/Degradation of Polymer Solar Cells. *Sol. Energy Mater. Sol. Cells* **2008**, *92*, 686–714.
- (12) Tao, C.; Ruan, S.; Xie, G.; Kong, X.; Shen, L.; Meng, F.; Liu, C.; Zhang, X.; Dong, W.; Chen, W. Role of Tungsten Oxide in Inverted Polymer Solar Cells. *Appl. Phys. Lett.* **2009**, *94*, 043311.
- (13) Irwin, M. D.; Buchholz, D. B.; Hains, A. W.; Chang, R. P.; Marks, T. J. p-Type Semiconducting Nickel Oxide as an Efficiency-Enhancing Anode Interfacial Layer in Polymer Bulk-Heterojunction Solar Cells. *Proc. Natl. Acad. Sci. U. S. A.* **2008**, *105*, 2783–2787.
- (14) Sun, Y.; Takacs, C. J.; Cowan, S. R.; Seo, J. H.; Gong, X.; Roy, A.; Heeger, A. J. Efficient, Air-Stable Bulk Heterojunction Polymer Solar Cells Using MoO_x as the Anode Interfacial Layer. *Adv. Mater.* **2011**, *23*, 2226–2230.
- (15) Shrotriya, V.; Li, G.; Yao, Y.; Chu, C.-W.; Yang, Y. Transition Metal Oxides as the Buffer Layer for Polymer Photovoltaic Cells. *Appl. Phys. Lett.* **2006**, *88*, 073508.
- (16) Kim, J. Y.; Kim, S. H.; Lee, H. H.; Lee, K.; Ma, W.; Gong, X.; Heeger, A. J. New Architecture for High-Efficiency Polymer Photovoltaic Cells Using Solution-Based Titanium Oxide as an Optical Spacer. *Adv. Mater.* **2006**, *18*, 572–576.
- (17) White, M.; Olson, D.; Shaheen, S.; Kopidakis, N.; Ginley, D. S. Inverted Bulk-Heterojunction Organic Photovoltaic Device Using a Solution-Derived ZnO Underlayer. *Appl. Phys. Lett.* **2006**, *89*, 143517.
- (18) Jo, S. B.; Lee, J. H.; Sim, M.; Kim, M.; Park, J. H.; Choi, Y. S.; Kim, Y.; Ihn, S. G.; Cho, K. High Performance Organic Photovoltaic Cells Using Polymer-Hybridized ZnO Nanocrystals as a Cathode Interlayer. *Adv. Energy Mater.* **2011**, *1*, 690–698.
- (19) Hu, T.; Li, F.; Yuan, K.; Chen, Y. Efficiency and Air-Stability Improvement of Flexible Inverted Polymer Solar Cells Using ZnO/Poly (Ethylene Glycol) Hybrids as Cathode Buffer Layers. *ACS Appl. Mater. Interfaces* **2013**, *5*, 5763–5770.
- (20) Yang, T.; Wang, M.; Duan, C.; Hu, X.; Huang, L.; Peng, J.; Huang, F.; Gong, X. Inverted Polymer Solar Cells with 8.4% Efficiency by Conjugated Polyelectrolyte. *Energy Environ. Sci.* **2012**, *5*, 8208–8214.
- (21) Chang, Y.-M.; Leu, C.-Y. Conjugated Polyelectrolyte and Zinc Oxide Stacked Structure as an Interlayer in Highly Efficient and Stable Organic Photovoltaic Cells. *J. Mater. Chem. A* **2013**, *1*, 6446–6451.
- (22) Zuo, L.; Gu, Z.; Ye, T.; Fu, W.; Wu, G.; Li, H.; Chen, H. Enhanced Photovoltaic Performance of CH₃NH₃PbI₃ Perovskite Solar Cells through Interfacial Engineering Using Self-Assembling Monolayer. *J. Am. Chem. Soc.* **2015**, *137*, 2674–2679.
- (23) Hu, Q.; Liu, Y.; Li, Y.; Ying, L.; Liu, T.; Huang, F.; Wang, S.; Huang, W.; Zhu, R.; Gong, Q. Efficient and Low-Temperature Processed Perovskite Solar Cells Based on a Cross-Linkable Hybrid Interlayer. *J. Mater. Chem. A* **2015**, *3*, 18483–18491.
- (24) Liu, S.; Zhang, K.; Lu, J.; Zhang, J.; Yip, H.-L.; Huang, F.; Cao, Y. High-Efficiency Polymer Solar Cells Via the Incorporation of an Amino-Functionalized Conjugated Metallocopolymer as a Cathode Interlayer. *J. Am. Chem. Soc.* **2013**, *135*, 15326–15329.
- (25) Wang, G.; Jiu, T.; Tang, G.; Li, J.; Li, P.; Song, X.; Lu, F.; Fang, J. Interface Modification of ZnO-Based Inverted PTB7:PC₇₁BM Organic Solar Cells by Cesium Stearate and Simultaneous Enhancement of Device Parameters. *ACS Sustainable Chem. Eng.* **2014**, *2*, 1331–1337.
- (26) Wu, Y.; Zhang, W.; Li, X.; Min, C.; Jiu, T.; Zhu, Y.; Dai, N.; Fang, J. Solution-Processed Hybrid Cathode Interlayer for Inverted Organic Solar Cells. *ACS Appl. Mater. Interfaces* **2013**, *5*, 10428–10432.
- (27) Dona, J.; Herrero, J. Process and Film Characterization of Chemical-Bath-Deposited ZnS Thin Films. *J. Electrochem. Soc.* **1994**, *141*, 205–210.
- (28) Fang, X.-S.; Ye, C.-H.; Zhang, L.-D.; Wang, Y.-H.; Wu, Y.-C. Temperature-Controlled Catalytic Growth of ZnS Nanostructures by the Evaporation of ZnS Nanopowders. *Adv. Funct. Mater.* **2005**, *15*, 63–68.
- (29) Fang, X.; Bando, Y.; Shen, G.; Ye, C.; Gautam, U. K.; Costa, P. M.; Zhi, C.; Tang, C.; Golberg, D. Ultrafine ZnS Nanobelts as Field Emitters. *Adv. Mater.* **2007**, *19*, 2593–2596.
- (30) Bredol, M.; Matras, K.; Szatkowski, A.; Sanetra, J.; Prodi-Schwab, A. P3HT/ZnS: a New Hybrid Bulk Heterojunction Photovoltaic System with Very High Open Circuit Voltage. *Sol. Energy Mater. Sol. Cells* **2009**, *93*, 662–666.
- (31) Maier, E.; Fischereder, A.; Haas, W.; Mauthner, G.; Albering, J.; Rath, T.; Hofer, F.; List, E. J.; Trimmel, G. Metal Sulfide-Polymer Nanocomposite Thin Films Prepared by a Direct Formation Route for Photovoltaic Applications. *Thin Solid Films* **2011**, *519*, 4201–4206.
- (32) Kuwabara, T.; Nakamoto, M.; Kawahara, Y.; Yamaguchi, T.; Takahashi, K. Characterization of ZnS-Layer-Inserted Bulk-Heterojunction Organic Solar Cells by AC Impedance Spectroscopy. *J. Appl. Phys.* **2009**, *105*, 124513.
- (33) Traverse, C. J.; Young, M.; Wagner, S.; Zhang, P.; Askeland, P.; Barr, M. C.; Lunt, R. R. Efficient Zinc Sulfide Cathode Layers for Organic Photovoltaic Applications via n-Type Doping. *J. Appl. Phys.* **2014**, *115*, 194505.
- (34) Ikeda, T.; Hagihara, H. The Crystal Structure of Zinc Ethylxanthate. *Acta Crystallogr.* **1966**, *21*, 919–927.
- (35) Hunt, M.; Kruger, A.; Smith, L.; Winter, G. CO, CS, and MS Vibration Frequencies of Metal Xanthates. *Aust. J. Chem.* **1971**, *24*, 53–57.
- (36) Elumalai, N. K.; Jin, T. M.; Chellappan, V.; Jose, R.; Palaniswamy, S. K.; Jayaraman, S.; Raut, H. K.; Ramakrishna, S. Electrospun ZnO Nanowire Plantations in the Electron Transport Layer for High-Efficiency Inverted Organic Solar Cells. *ACS Appl. Mater. Interfaces* **2013**, *5*, 9396–9404.
- (37) Fabregat-Santiago, F.; Bisquert, J.; Garcia-Belmonte, G.; Boschloo, G.; Hagfeldt, A. Influence of Electrolyte in Transport and Recombination in Dye-Sensitized Solar Cells Studied by Impedance Spectroscopy. *Sol. Energy Mater. Sol. Cells* **2005**, *87*, 117–131.
- (38) Fabregat-Santiago, F.; Bisquert, J.; Palomares, E.; Otero, L.; Kuang, D.; Zakeeruddin, S. M.; Grätzel, M. Correlation Between Photovoltaic Performance and Impedance Spectroscopy of Dye-Sensitized Solar Cells Based on Ionic Liquids. *J. Phys. Chem. C* **2007**, *111*, 6550–6560.
- (39) He, Z.; Zhong, C.; Huang, X.; Wong, W. Y.; Wu, H.; Chen, L.; Su, S.; Cao, Y. Simultaneous Enhancement of Open-Circuit Voltage, Short-Circuit Current Density, and Fill Factor in Polymer Solar Cells. *Adv. Mater.* **2011**, *23*, 4636–4643.
- (40) Liang, Y.; Xu, Z.; Xia, J.; Tsai, S. T.; Wu, Y.; Li, G.; Ray, C.; Yu, L. For the Bright Future-Bulk Heterojunction Polymer Solar Cells with Power Conversion Efficiency of 7.4%. *Adv. Mater.* **2010**, *22*, E135–E138.
- (41) Tao, C.; Ruan, S.; Zhang, X.; Xie, G.; Shen, L.; Kong, X.; Dong, W.; Liu, C.; Chen, W. Performance Improvement of Inverted Polymer Solar Cells with Different Top Electrodes by Introducing a MoO₃ Buffer Layer. *Appl. Phys. Lett.* **2008**, *93*, 193307.
- (42) Li, X.; Zhang, W.; Wu, Y.; Min, C.; Fang, J. High Performance Polymer Solar Cells with a Polar Fullerene Derivative as the Cathode Buffer Layer. *J. Mater. Chem. A* **2013**, *1*, 12413–12416.
- (43) Lee, B. R.; Jung, E. D.; Nam, Y. S.; Jung, M.; Park, J. S.; Lee, S.; Choi, H.; Ko, S. J.; Shin, N. R.; Kim, Y. K.; et al. Amine-Based Polar Solvent Treatment for Highly Efficient Inverted Polymer Solar Cells. *Adv. Mater.* **2014**, *26*, 494–500.
- (44) Chu, T.-Y.; Song, O.-K. Hole Mobility of N, N'-bis (naphthalen-1-yl)-N, N'-Bis (phenyl) Benzidine Investigated by Using Space-Charge-Limited Currents. *Appl. Phys. Lett.* **2007**, *90*, 203512.
- (45) Naka, S.; Okada, H.; Onnagawa, H.; Tsutsui, T. High Electron Mobility in Bathophenanthroline. *Appl. Phys. Lett.* **2000**, *76*, 197–199.
- (46) Ichikawa, M.; Amagai, J.; Horiba, Y.; Koyama, T.; Taniguchi, Y. Dynamic Turn-on Behavior of Organic Light-Emitting Devices with Different Work Function Cathode Metals under Fast Pulse Excitation. *J. Appl. Phys.* **2003**, *94*, 7796–7800.